# SIMULATION OF UNSTEADY FLOW PAST TAPERED CIRCULAR CYLINDERS USING AN IMMERSED BOUNDARY METHOD

**Vagesh D. Narasimhamurthy[†], Florian Schwertfirm[‖], Helge I. Andersson[†] and Bjørnar Pettersen[§]**

[†]Norwegian University of Science and Technology (NTNU), Dept. of Energy and Process Engineering, NO-7491 Trondheim, Norway
e-mail: vagesh.d.narasimhamurthy@ntnu.no

[‖]Technische Universität München, Fachgebiet Hydromechanik, 80333 Munich, Germany

[§]Norwegian University of Science and Technology (NTNU), Dept. of Marine Technology, NO-7491 Trondheim, Norway

**Key words:** Cellular vortex shedding, Tapered cylinder, Immersed Boundary Method, Oblique vortex shedding

**Abstract.** *Three-dimensional numerical calculations of laminar vortex shedding behind a linearly tapered circular cylinder with taper ratio 75:1 have been carried out at a Reynolds number 131 (based on the large diameter and the uniform inflow velocity) using a Finite Volume code. Computations were performed on a staggered-Cartesian grid and a direct forcing Immersed Boundary Method (IBM) was used to transform the boundary condition at the solid surface into internal boundary conditions at the nodes of the Cartesian grid. Results showed a pattern of discrete oblique shedding cells, which included both vortex dislocation and vortex splitting. The local Strouhal number versus local Reynolds number curve showed excellent qualitative agreement with the experimental results reported by Piccirillo and Van Atta in 1993. However, quantitative deviations exist between the two techniques. Numerical noise (oscillations) was observed along the span in the steady flow calculation with Reynolds number 40, the reason for which has to be further investigated. The overall computational performance of the IBM proved to be very promising when compared to the boundary fitted or unstructured grid solvers.*

## 1 INTRODUCTION

Three-dimensional (3-D) vortex shedding may occur in the wake of a circular cylinder for three fundamentally different reasons: i) the vortex dynamics in the wake may be intrinsically three-dimensional, ii) the inflow may be non-uniform, and iii) the cylinder geometry may itself be non-uniform. In the present paper we focus on the latter category,

i.e. on the three-dimensionalisation induced by a spanwise variation of the cylinder diameter. Tapered cylinders are basically truncated cones and are of great practical relevance (e.g., oil-platform legs, chimneys and light houses). They offer a geometrically simple configuration with complex flow physics in the near wake. Depending on the taper ratio ($R_T = l/(d_2 - d_1)$; where $l$ is the length of the circular cylinder and $d_2$ and $d_1$ denote the diameter of its wide and narrow ends, respectively) the variation of local Reynolds number along the span of the cylinder may produce a range of distinct flow-regimes (e.g., steady wake, laminar unsteady wake and turbulent wake) exist side by side in the same geometry.

Until recently, the majority of numerical calculations of the flow over tapered cylinders were performed using boundary-fitted grids (Jespersen & Levit[1] and Vallès et al.[2] have performed calculations in the laminar unsteady wake regime) but solvers for curvilinear or unstructured grids are less efficient than Cartesian solvers in terms of computational time and memory requirements[11]. Recently Parnaudeau et al.[3,4] have performed turbulent flow calculations using a direct forcing Immersed Boundary Method (IBM). However their Reynolds number $Re_2$ (based on the large diameter $d_2$ and the uniform inflow velocity $U$) was in another range compared to the present investigation. Vallès et al.[2] have carried out flow calculations for two different $R_T$ (75:1 and 100:1) and in the $Re_2$ range 131-178. They found that the numerical results compared surprisingly well with the extensive laboratory experiments reported by Piccirillo & Van Atta[5]. However, the predicted variation of local Strouhal number ($St_{local} = f_s d_{local}/U$; where $f_s$ is the shedding frequency) versus local Reynolds number ($Re_{local} = U d_{local}/\nu$) did not match the curve fit $St = 0.195 - 5.0/Re$ deduced from the laboratory experiments[5]. In the present study we used a direct forcing IBM[6,7] to clarify some deviations between the simulations and the experiments. A detailed investigation of numerical noise level and its origin was carried out by studying steady-flow over the cylinder at $Re_2 = 40$.

## 2   FLOW CONFIGURATION AND PARAMETERS

The computational domain was as shown in figure 1. All dimensions were normalised by the diameter at the wide end ($d_2 = 1$). The normalised diameter at the narrow end was $d_1 = 0.556$ and the length of the cylinder was $l = 33.461$. The taper ratio of the cylinder was defined as,

$$R_T = \frac{l}{(d_2 - d_1)} = 75 : 1 \qquad (1)$$

and was the same in both cases considered. The Reynolds number based on the uniform inflow velocity ($U = 1$) and the diameters at wide, narrow and center-span ($d_{cs} = 0.778$) of the cylinder for both laminar unsteady wake and steady wake flow were as shown in Table 1. The kinematic viscosity was therefore different in the two cases. The Reynolds numbers were well below 190 at which the intrinsic 'mode A' instability is known to occur in otherwise two-dimensional configurations.
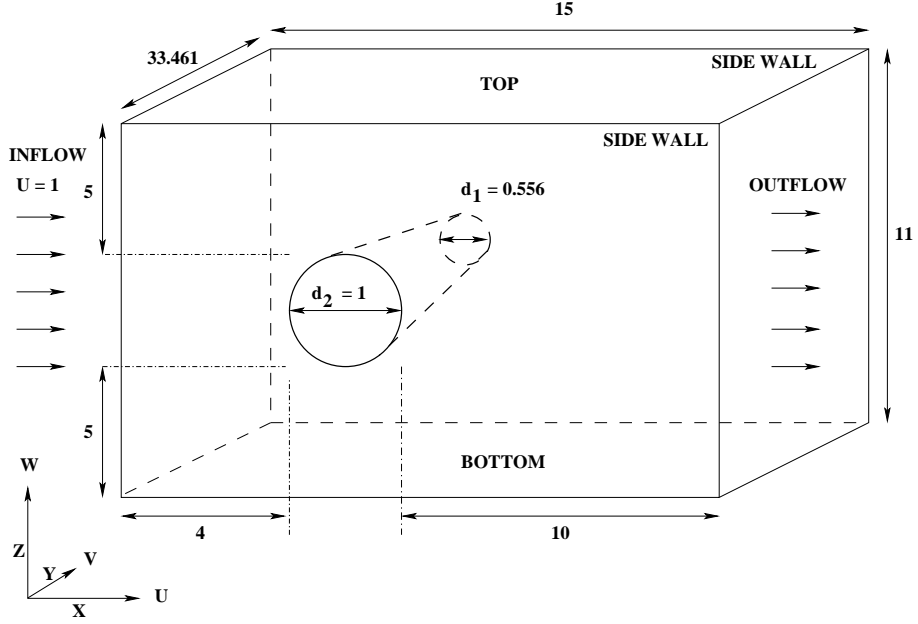
Figure 1: Computational domain (not to scale)

| Case | Re$_2$ | Re$_1$ | Re$_{cs}$ |
|---|---|---|---|
| Laminar unsteady wake | 131 | 72.83 | 101.91 |
| Steady wake | 40 | 22.24 | 31.12 |

Table 1: Reynolds number

## 3 NUMERICAL METHOD

### 3.1 Instantaneous equations of motion

All fluid motions of Newtonian fluids (where the continuum approximation is valid) are governed by a system of dynamical equations, namely the Navier Stokes (N-S) equations. For incompressible flows, the N-S equations reduce to,

$$\frac{\partial \tilde{u}_j}{\partial \tilde{x}_j} = 0 \tag{2}$$

$$\left[ \frac{\partial \tilde{u}_i}{\partial t} + \tilde{u}_j \frac{\partial \tilde{u}_i}{\partial x_j} \right] = -\frac{1}{\rho} \frac{\partial \tilde{p}}{\partial x_i} + \nu \frac{\partial^2 \tilde{u}_i}{\partial x_j \partial x_j} \tag{3}$$

where, $\tilde{u}_i = \tilde{u}_i(\vec{x}, t)$, is a function of space $\vec{x}$ and time $t$ and $\nu$ and $\rho$ denote the kinematic viscosity and the density of the fluid.

### 3.2 Numerical schemes, the solver and the grid

The governing equations were solved in 3-D space and time using a Finite Volume code[8,9]. The code uses staggered Cartesian grid arrangement. Time marching was carried

3

out using a $3^{rd}$ order explicit Runge-Kutta scheme for the momentum equations and an iterative SIP (Strongly Implicit Procedure) solver[10] for the Poisson equation. Spatial discretization was carried out using a $2^{nd}$ order central-differencing scheme. In all the computations we employed non-equidistant Cartesian grids in X-Z plane. Equidistant grid points were used in Y-direction. As an example a fine mesh of $3.3 \times 10^6$ grid points is shown in Figure 2. In grid generation care was taken to have a sufficient number of grid points upstream of the cylinder, in order to capture the Hiemenz-like boundary layer[14] at the stagnation point. The boundary layer thickness $\delta$ was given by,

$$\delta = \frac{1.2d}{\sqrt{Re_d}} \tag{4}$$

where, $d$ is the local diameter at any span-wise position and $Re_d$ is the Reynolds number based on $d$. The boundary layer thickness $\delta$ for both unsteady and steady cases was estimated as shown in Table 2.

| Case | $\delta_2$ | $\delta_1$ |
|---|---|---|
| Laminar unsteady wake | 0.10484 | 0.07808 |
| Steady wake | 0.18973 | 0.14147 |

Table 2: Hiemenz boundary layer thickness in the stagnation zone

## 3.3 Boundary conditions

Boundary conditions were as shown in Table 3. A uniform inflow velocity profile $U = 1$ was fixed at the inlet. Convective and diffusive fluxes were set to zero on both sides and top and bottom (see figure 1). At the outflow, Neumann boundary condition was used for velocities and pressure was set to zero. The no-slip boundary condition on the cylinder body was implemented by using a direct forcing IBM which will be discussed in the following section.

| Face | Boundary condition |
|---|---|
| Inflow | $U = 1; V = W = 0; \partial P/\partial X = 0$ |
| Side walls | $V = 0; \partial U/\partial Y = \partial W/\partial Y = \partial P/\partial Y = 0$ |
| Top and Bottom walls | $W = 0; \partial U/\partial Z = \partial V/\partial Z = \partial P/\partial Z = 0$ |
| Outflow | $\partial U/\partial X = \partial V/\partial X = \partial W/\partial X = 0; P = 0$ |

Table 3: Boundary conditions

## 4   IMMERSED BOUNDARY METHOD

In the present computation we used a *direct forcing* IBM[6,7] to transform the boundary condition at the solid cylindrical surface into internal boundary conditions at the nodes of the Cartesian grid. The forcing is called *direct* because the boundary condition remains
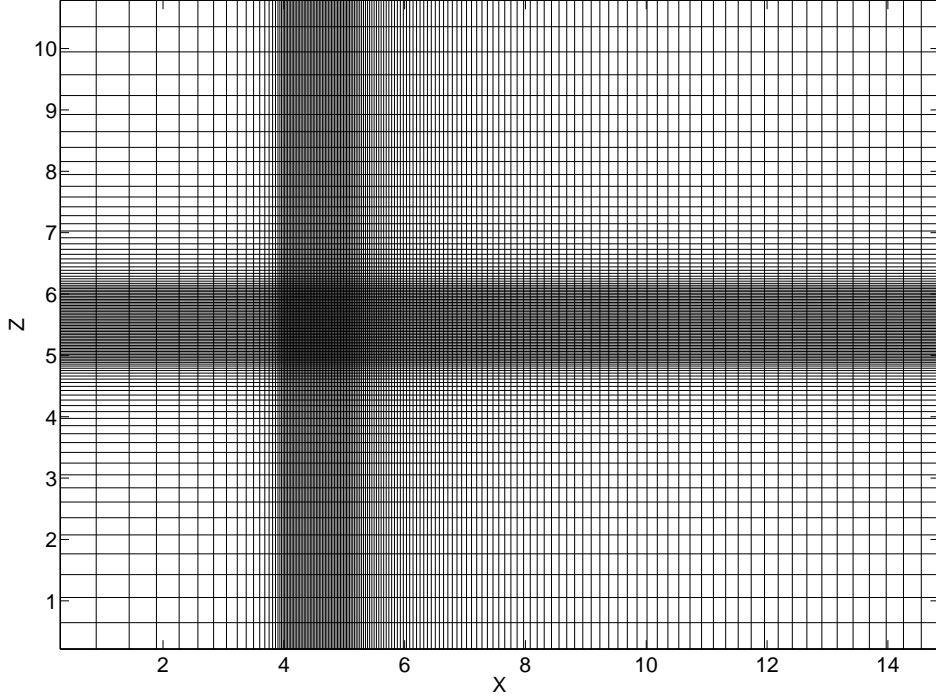
Figure 2: Mesh in X-Z plane: $3.3 \times 10^6$ grid points in total ($[N_X \times N_Y \times N_Z] = [150 \times 200 \times 110]$)

the same at each time step regardless of the characteristic frequencies of the flow (see Iaccarino & Verzicco[12] and Mittal & Iaccarino[13] for an extensive review of different IBMs). Direct forcing is practically the same as enforcing the boundary condition within the flow. When the boundary does not coincide with Cartesian grid points, an interpolation is required. Thus the accuracy of IBM depends on the interpolation technique, the order of interpolation and the direction of interpolation. In this section we discuss the blocking algorithm and the interpolation technique used.

## 4.1 Blocking algorithm

The cylinder surface to be immersed in the Cartesian mesh was represented by a mesh consisting of triangles. The blocking of the Cartesian cells intersected by these triangles was carried out as follows:

i) The intersection points of triangle surface and the coordinate line passing through the pressure cell center were identified. The pressure cells containing those intersection points were blocked, as shown in Figure 3.

ii) In the second sweep all the pressure cells within the blocked surface were blocked.

iii) Finally all the velocity cells corresponding to blocked pressure cells were blocked.
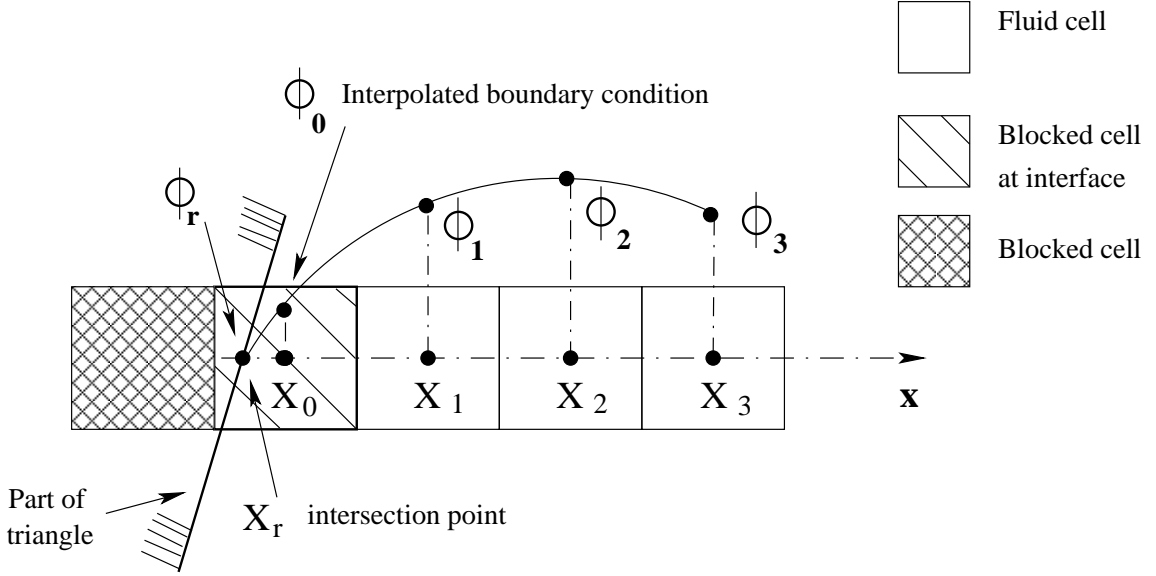
5

Figure 3: 1-Dimensional stencil configuration for interpolation in x-direction

All these blocked cells were marked inactive and were excluded from certain steps in the time-marching algorithm (e.g., convergence check).

## 4.2   Interpolation technique

In Figure 3, $\phi_0$ is the internal boundary condition value to be determined by interpolation. $X_r$ is the intersection point between the triangle and the coordinate line. $\phi_r$ is the value at $X_r$ which is known (the value on the wall). Thus by considering the neighbouring variables $\phi_i$ ($\phi_1$, $\phi_2$, $\phi_3$, $etc$) the stencils are formed. A general stencil formulation for $\phi_0$ looks like,

$$\phi_0 = (\sum_{i=1}^{N} \alpha_i.\phi_i) + \alpha_r.\phi_r \tag{5}$$

where, $N$ is the number of neighbouring cells involved in the interpolation. The interpolation coefficients $\alpha_i$ and $\alpha_r$ depend on the interpolation technique and geometry only and therefore were computed in a preprocessing step.

In the present simulation we used *least squares* interpolation of $3^{rd}$ order. The detailed derivation of this technique was explained in Peller et al.[6]. Using matrix stability analysis they studied the numerical stability of higher-order *Lagrange* and *least squares* interpolation and concluded that *least squares* interpolation of $3^{rd}$ order is very robust and numerically stable. Higher-order interpolation may indeed avoid strong grid-clustering in the wall vicinity but may not increase the accuracy of the solver (the spatial accuracy of the solver was $2^{nd}$ order as discussed in previous section). The stencil in each direction was 1-dimensional but Tremblay et al.[7] have employed *weighting* to account for three

dimensionality.

## 5   RESULTS AND DISCUSSION

### 5.1   Laminar unsteady flow

The unsteady flow calculations were carried out with two different grid resolutions. Table 4 illustrates the mesh parameters. $N_X$, $N_Y$, and $N_Z$ correspond to the number of grid points in X, Y, and Z directions, respectively. Similarly $N_{US}$ and $N_{DS}$ correspond to the number of grid points upstream the cylinder and downstream the cylinder. $\Delta_{cyl}$ represents the grid cell size close to the cylinder in both X and Z directions.

| Case | Nodes | $N_X$ | $N_Y$ | $N_Z$ | $N_{US}$ | $N_{DS}$ | $\Delta_{cyl}$ |
|---|---|---|---|---|---|---|---|
| Coarse mesh | $1.2\times10^6$ | 120 | 100 | 100 | 20 | 80 | 0.05 |
| Fine mesh | $3.3\times10^6$ | 150 | 200 | 110 | 20 | 90 | 0.025 |

Table 4: Grid parameters

The time step $\Delta t = 0.005$ was found to assure stability and appropriate both with respect to the CFL condition and von Neumann analysis. The coarse-mesh computations were performed on a single processor Linux-PC (Intel P4-3.2GHz with 1GB RAM) and the fine-mesh on 15 processors of SGI Origin 3800. A detailed comparison of computational performance of the present simulations and that of Vallès et al.[2] is shown in Table 5. A noteworthy distinction is that Vallès et al.[2] used an implicit time-stepping.

| Case | Computer | Nodes | $\Delta t$ | Iterations/$\Delta t$ | cpu$\frac{s}{\Delta t}$ |
|---|---|---|---|---|---|
| Coarse mesh | Linux PC | $1.2\times10^6$ | 0.005 $d_2$/U | 15 | 3.9 |
| Fine mesh | SGI Origin 3800 | $3.3\times10^6$ | 0.005 $d_2$/U | 15 | 90 |
| Vallès et al.[2] | Cray T3E | $0.256\times10^6$ | 0.1 $d_2$/U | 20 | 3060 |

Table 5: Computational performance

Flow visualization of 3-D vortex shedding could be carried out in many ways. In figure 4 and figure 5 the time evolution of the pressure along the span for both coarse mesh and fine mesh has been plotted. The instantaneous pressure was sampled along a line parallel to the axis of the cylinder located $2d_{cs}$ downstream the axis in X-direction and $1d_{cs}$ offset in Z-direction. The offset in Z-direction was carried out to detect only one side of the vortex street. An initial comparison between the two figures itself indicate the complex flow structure and vortex splitting. Both figures show a nearly periodic occurence of vortex splitting around the center span of the cylinder. However, this phenomenon of periodic occurence of vortex cells was more evident in the coarse mesh simulation. This could be due to the inability of the coarse mesh to capture the instabilities along the span. It should also be noted that the vortex shedding was more oblique in the fine mesh than on the coarse mesh. This point was further justified in figure 6, where iso-pressure contours for the fine mesh clearly indicate the larger shedding angle compared to the coarse mesh.
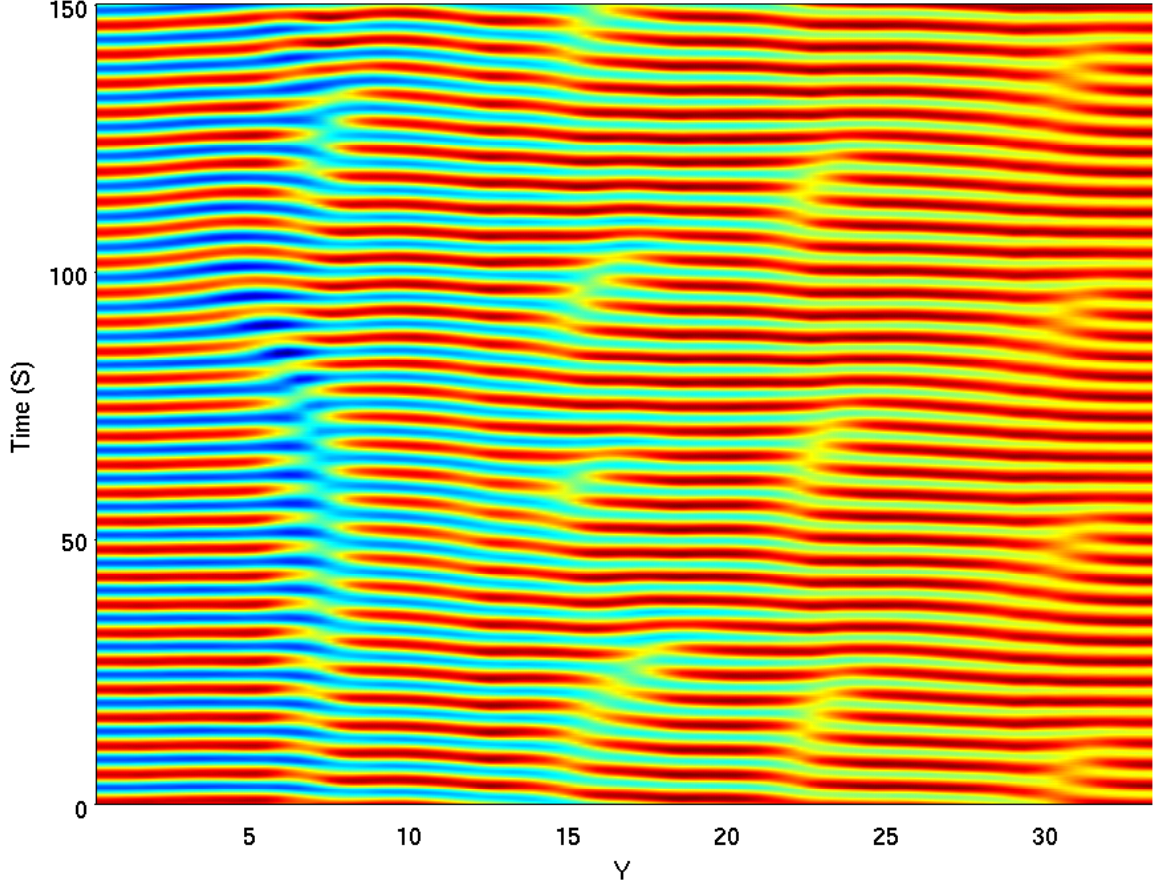
Figure 4: Time evolution of the pressure along the entire span: Coarse mesh

However further qualitative investigations were carried out by spectral analysis of pressure time traces.

Our primary objective was to investigate the significant deviations in the $St_{local}$ versus $Re_{local}$ curve between simulations[2] and experiments[5] and therefore the power spectrum of pressure time traces were investigated. In figure 7 Piccirillo & Van Atta's[5] curve-fit $St = 0.195 - 5.0/Re$ along with Williamson & Brown's[15] universal $St$-$Re$ curve for straight uniform circular cylinders given by,

$$St = A + \frac{B}{\sqrt{Re}} + \frac{C}{Re} \tag{6}$$

where, $A = 0.2850, B = -1.3897$ and $C = 1.8061$, were plotted together with numerical results. (Note: In Vallès et al.[2] the present case corresponds to their *Case B*, which accidentally was mis-labelled as *Case C* in their *St-Re* figure) Both our coarse and fine
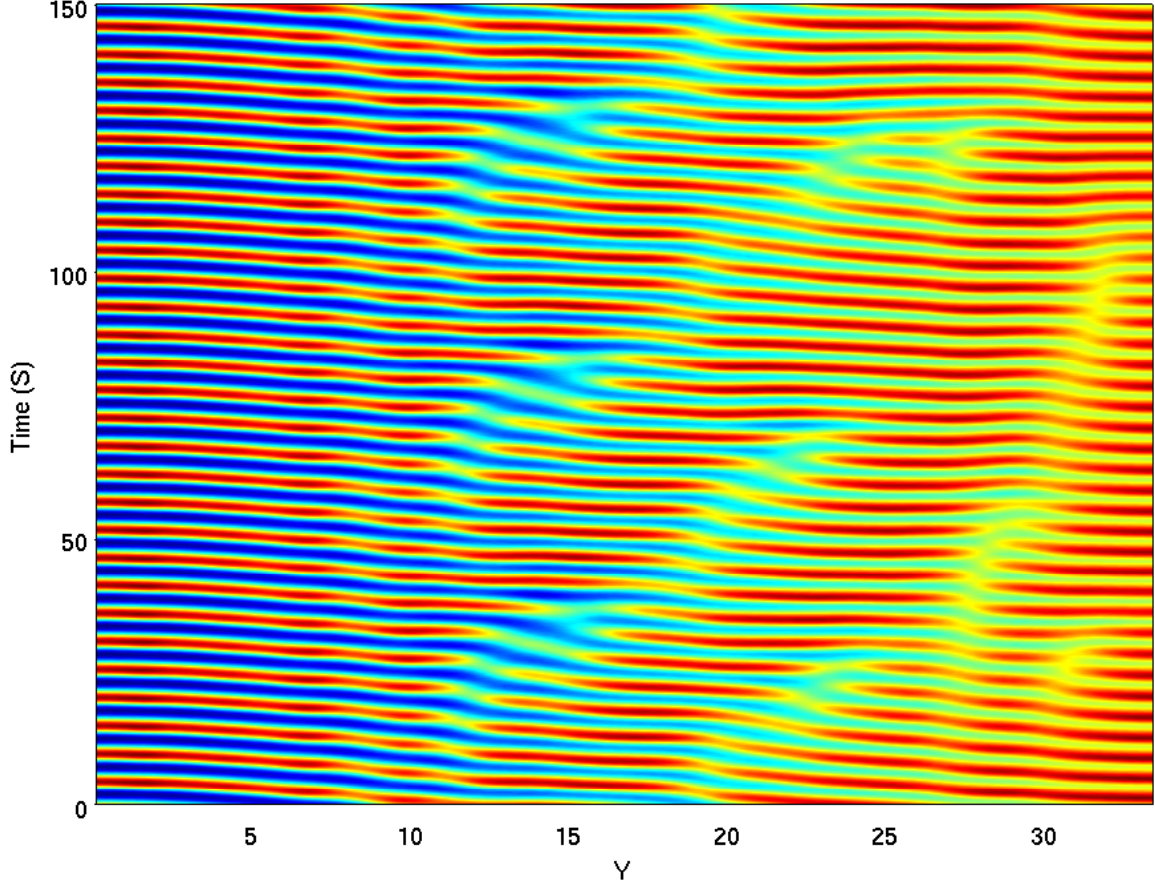
8

Figure 5: Time evolution of the pressure along the entire span: Fine mesh

mesh simulations clearly captured the distinct shedding cells with constant shedding frequency and fine splitting. It should be worth to mention here that our *St-Re* curve was very sensitive to the sampling time and we sampled the instantaneous pressure for nearly 300 $d_2/U$ to get reliable statistics. Even though our simulations qualitatively reproduced what have been observed in the laboratory there still exists quantitative deviations both from the experiments[5] and the earlier simulation[2]. However, the trend of all computer simulations is similar. It should be noted that the experimental curve-fit was based on the Strouhal number values at the centre of each shedding cell (cell-center Strouhal number), whereas all the numerical results were based on a truly local Strouhal number for each spanwise location. In figure 8 shedding cell mid-point locations were compared with both experiment and other numerical results. Here also significant quantitative deviations exist between the different techniques. One possible reason could be the difference in boundary conditions in the laboratory set-up and computer calculations. However a further step
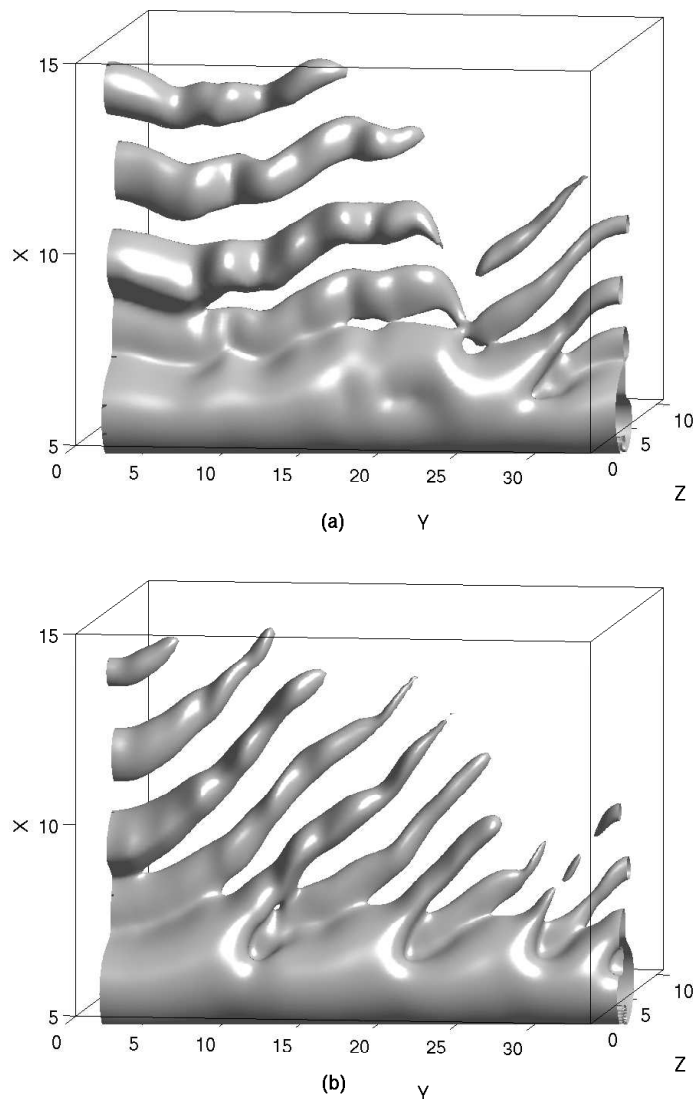
9

Figure 6: 3-dimensional iso-pressure contours. Contour level $\tilde{p} = -0.1$. (a)coarse mesh; (b)fine mesh. The flow direction is from bottom to top.

was taken to investigate the accuracy of our present approach by simulating a steady flow over the same configuration.

## 5.2 Steady flow

Steady flow calculations were performed with the same computational configuration as above by reducing $Re_2$ to 40. The flow was simulated only with the fine mesh. The objective was to avoid the unsteady effects and focus only on the numerical noise (if any). The spanwise numerical oscillations (if any) were studied by comparing the non-
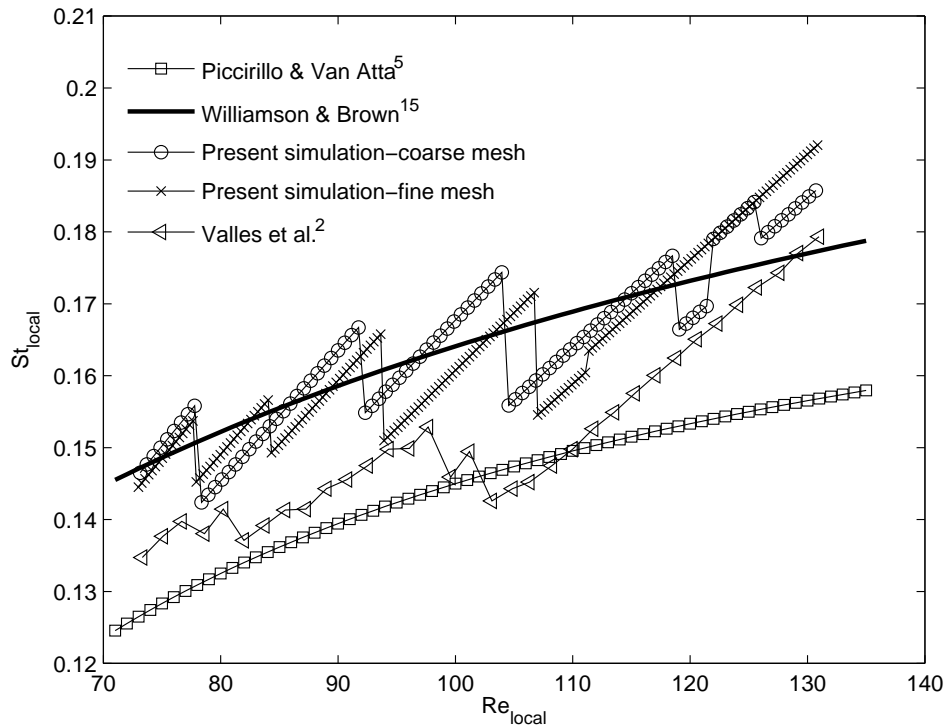
10

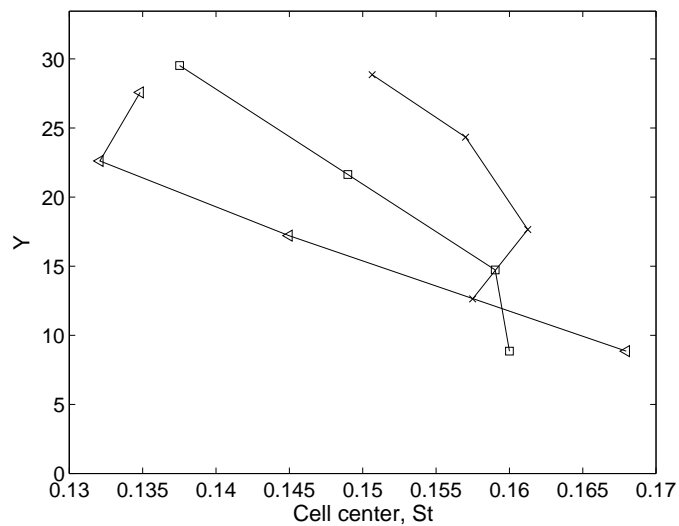Figure 7: $St_{local}$ versus $Re_{local}$



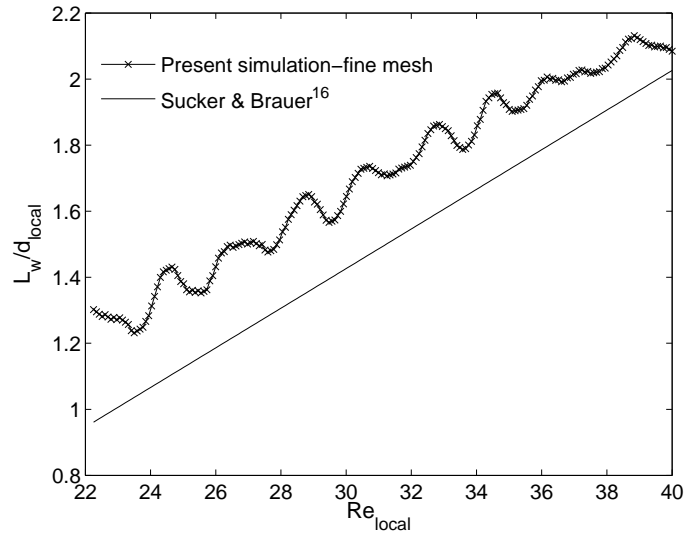Figure 8: Shedding cell mid-point locations. Symbols are the same as in figure 7

11

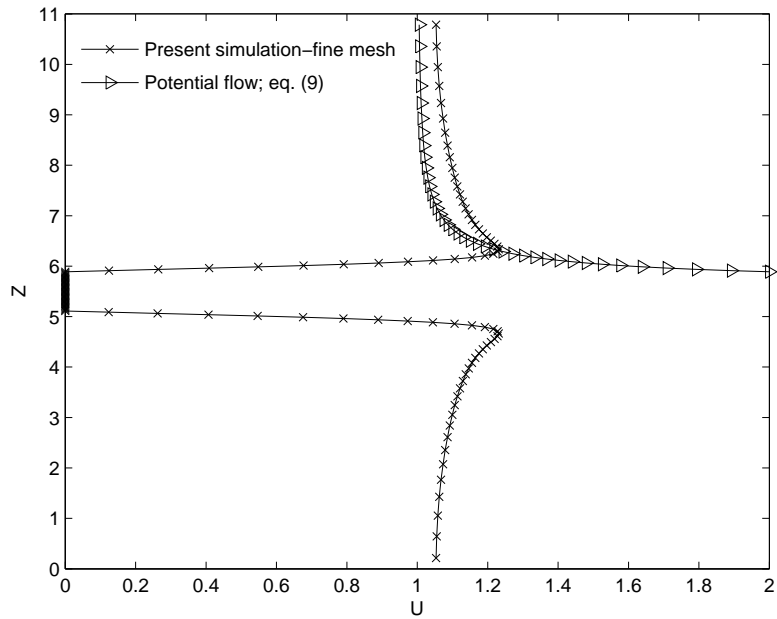Figure 9: Non-dimensional steady wake length along the span



Figure 10: Variation of the streamwise velocity (U) profile in the cross-stream (Z) direction at X = 4.5 and Y = 16.7 (center-span of the cylinder)

dimensional bubble or wake length ($L_w/d_{local}$) for each spanwise position with Sucker & Brauer's[16] empirical curve fit for straight uniform circular cylinders. The empirical

12

relation was given by,

$$\frac{L_w}{d_{local}} = 0.12 Re_{local} - 0.748 \qquad (7)$$

From figure 9, it is clear that small oscillations do exist in the span-wise direction even though the trend is excellent. Our initial guess was that the oscillations were due to the grid resolution close to the cylinder surface being some what too coarse. It should be noted that the difference between the two radii, $(d_2 - d_1)/2 = 0.222$, was very small compared to the length $l$ of the cylinder. Given the grid aspect ratio restrictions, this would mean a high demand on the mesh. This demand on the mesh refinement would in turn lead to a grid-clustering around the cylinder. However this guess has to be further investigated.

In figure 10 the computed laminar boundary layer profile is compared to the potential flow calculations. From potential theory, the stream function $\psi$ for flow past a circular cylinder without rotation was given by (see White[17]),

$$\psi = U sin\theta(r - \frac{a^2}{r}) \qquad (8)$$

where $a$ is the radius of the cylinder and $r$ any distance from the axis of the cylinder. Here $\theta = 90^o$ corresponds to the Y-Z plane passing through the center of the cylinder. Thereby the velocity component $U_\theta$ becomes,

$$U_\theta = -\frac{\partial \psi}{\partial r} = -U sin\theta(1 + \frac{a^2}{r^2}) = -(1 + \frac{a^2}{r^2}) \qquad (9)$$

The symmetry and smoothness of the flow in the boundary layer on either side of the cylinder were well captured in the simulation. However, the numerical results do not collapse with the irrotational velocity profile far from the cylinder, a reason for which could be that the potential flow assumption holds good for high Reynolds number flows. Another reason (less probable) could be that our computational box in Z-direction is slightly too narrow.

## 6  CONCLUSIONS

i) The computational performance of the IBM proved to be very promising when compared to the boundary fitted and unstructured grid solvers, especially the computations on the Linux PC with $1.2 \times 10^6$ grid points was surprisingly fast.

ii) Complex flow structures as observed in experiments[5], including vortex splitting and vortex dislocation, were successfully reproduced using IBM.

iii) $St_{local}$ versus $Re_{local}$ curve showed excellent qualitative agreement with the experiments. However, quantitative deviations exist between the two techniques. It should be

noted that end effects were negligible in our case and the boundary conditions in the numerical simulation and in the laboratory were therefore different.

iv) Numerical oscillations along the span were observed in the steady flow calculation, the reason for which has to be further investigated.

## ACKNOWLEDGEMENTS

## REFERENCES

[1] D.C. Jespersen and C. Levit, "Numerical simulation of flow past a tapered cylinder", *AIAA paper*, **91-0751**, (1991).

[2] B. Vallès, H.I. Andersson and C.B. Jenssen, "Oblique vortex shedding behind tapered cylinders", *J. Fluids Struct.*, **16**, 453-463, (2002).

[3] P. Parnaudeau, D. Heitz, E. Lamballais and J.H. Silvestrini, "Direct numerical simulations of vortex shedding behind cylinders with spanwise linear nonuniformity", *Proc. TSFP4*, 111-116, (2005).

[4] P. Parnaudeau, D. Heitz, E. Lamballais and J.H. Silvestrini, "Direct numerical simulations of vortex shedding behind cylinders with spanwise linear nonuniformity", *J. Turbulence*, submitted.

[5] P.S. Piccirillo and C.W. Van Atta, "An experimental study of vortex shedding behind linearly tapered cylinders at low Reynolds number", *J. Fluid Mech.*, **246**, 163-195, (1993).

[6] N. Peller, A. Le Duc, F. Tremblay and M. Manhart, "High-order stable interpolations for immersed boundary methods", *Int. J. Numer. Meth. Fluids*, in press.

[7] F. Tremblay, M. Manhart, R. Friedrich, "DNS and LES of flow around a circular cylinder at a subcritical Reynolds number with cartesian grids", *LES of Complex Transitional and Turbulent Flows*, Kluwer Academic Publishers, 133-150, (2001).

[8] M. Manhart, F. Tremblay and R. Friedrich, "MGLET: a parallel code for efficient DNS and LES of complex geometries", *Parallel Computational Fluid Dynamics 2000*, Elsevier Science B.V., 449-456, (2001).

[9] M. Manhart, "A zonal grid algorithm for DNS of turbulent boundary layers" , *Computers & Fluids*, **33**, 435-461, (2004).

[10] J.H. Ferziger and M. Peric, *Computational Methods for Fluid Dynamics*, Springer, (1996).

[11] R. Verzicco, J. Mohd-Yusof, P. Orlandi and D. Harworth, "LES in complex geometries using boundary body forces" , *In Proc. of the Summer Program 1998*, Center for Turbulence Research, Stanford, 171-186, (1998).

[12] G. Iaccarino and R. Verzicco, "Immersed boundary technique for turbulent flow simulations" , *Appl. Mech. Rev.*, **56**, 331-347, (2003).

[13] R. Mittal and G. Iaccarino, "Immersed boundary methods" , *Annu. Rev. Fluid Mech.*, **37**, 239-261, (2005).

[14] R.L. Panton, *Incompressible Flow*, Wiley-Interscience, $2^{nd}$ edition, (1997).

[15] C.H.K. Williamson and G.L. Brown, "A series in $1/\sqrt{Re}$ to represent the Strouhal-Reynolds number relationship of the cylinder wake" , *J. Fluids Struct.*, **12**, 1073-1085, (1998).

[16] D. Sucker and H. Brauer, "Fluiddynamik bei der angeströmten Zylindern", *Wärme- und Stoffübertragung*, **8**, (1975).

[17] F.M. White, *Fluid Mechanics*, McGraw-Hill International Editions, $2^{nd}$ edition, (1988).